

Nonlinear optical response of a two-dimensional quantum-dot supercrystal: Emerging multistability, periodic and aperiodic self-oscillations, chaos, and transient chaos

Igor V. Ryzhov,¹ Ramil F. Malikov,² Andrey V. Malyshev,^{3,4,*} and Victor A. Malyshev^{5,†}

¹ *Herzen State Pedagogical University, 191186 St. Petersburg, Russia*

² *Akmullah State Pedagogical University of Bashkortostan, 450000 Ufa, Russia*

³ *GISC, Departamento de Física de Materiales, Universidad Complutense, E-28040 Madrid, Spain*

⁴ *Ioffe Physical-Technical Institute, 26 Politechnicheskaya str., 194021 St. Petersburg, Russia*

⁵ *Zernike Institute for Advanced Materials, University of Groningen, Nijenborgh 4, 9747 AG Groningen, The Netherlands*



(Received 14 August 2019; published 16 September 2019)

We conduct a theoretical study of the nonlinear optical response of a two-dimensional semiconductor quantum-dot supercrystal subjected to a quasiresonant continuous-wave excitation. A constituent quantum dot is modeled as a three-level ladderlike system (comprising the ground, the one-exciton, and the biexciton states). To study the stationary response of the supercrystal, we propose an exact linear parametric method of solving the nonlinear steady-state problem, while to address the supercrystal optical dynamics qualitatively, we put forward a method to calculate the bifurcation diagram of the system. Analyzing the dynamics, we demonstrate that the supercrystal can exhibit multistability, periodic and aperiodic self-oscillations, and chaotic behavior, depending on parameters of the supercrystal and excitation conditions. The effects originate from the interplay of the intrinsic nonlinearity of quantum dots and the retarded interdot dipole-dipole interaction. The latter provides a positive feedback which results in the exotic supercrystal optical dynamics. These peculiarities of the supercrystal optical response open up a possibility for all-optical applications and devices. In particular, an all-optical switch, a tunable generator of THz pulses (in self-oscillating regime), a noise generator (in chaotic regime), and a tunable bistable mirror can be designed.

DOI: [10.1103/PhysRevA.100.033820](https://doi.org/10.1103/PhysRevA.100.033820)

I. INTRODUCTION

In the last decade, the so-called metamaterials, a class of new materials not existing in nature, received a great deal of attention (see for recent reviews Refs. [1–5]). Supercrystals comprising regularly spaced quantum emitters represent one of the examples of metamaterials with tunable optical properties which can be controlled by the geometry and chemical composition of components [6]. Modern nanotechnology has at its disposal a variety of methods to fabricate such systems [7–11]. In Fig. 1, a few examples of ultrathin sheets of regularly spaced semiconductor nanocrystals grown by the method of oriented attachment (see for details Ref. [7]) are present.

As is well known, a thin layer of two-level emitters (atoms, molecules, J aggregates), the thickness of which is much smaller than the radiation wavelength in the layer, can act as an all-optical bistable element [12–22]. For bistability to occur, two factors are required: nonlinearity of the material and a positive feedback. Interplay of these two factors leads to a situation when the system has two stable states; switching between them is governed again by an external optical signal. The nonlinearity of the layer is ensured by the fact that two-level emitters are nonlinear systems. The positive feedback originates from the secondary field, which is generated by the

emitters themselves; this is the so-called “intrinsic feedback,” i.e., here a cavity (external feedback) is not required.

A two-dimensional (2D) semiconductor quantum-dot (SQD) supercrystal represents a limiting case of a thin layer. In this paper, we conduct a theoretical study of the nonlinear optical response of such a system. A single SQD is considered as a pointlike system with three consecutive levels of the ground, one-exciton, and biexciton states (corresponding to the so-called ladder or cascade level scheme). Due to the high density of SQDs and high oscillator strengths of the SQD’s transitions, the total (retarded) dipole-dipole SQD-SQD interactions have to be taken into account, which is finally done in the mean-field approximation for the pointlike dipoles in a homogeneous host for simplicity. The real part of the dipole-dipole interaction results in the dynamic shift of the SQD’s energy levels, whereas the imaginary part describes the collective radiative decay of SQDs, both depending on the population differences between the levels. These two effects are crucial for the nonlinear dynamics of the SQD supercrystal. As a result, in addition to bistability, analogous to that for a thin layer of two-level emitters, we found multistability, periodic and aperiodic self-oscillation, and chaotic regimes in the optical response of the SQD supercrystal.¹ To the best of our knowledge, a detailed study of the SQD supercrystal

*Corresponding author: a.malyshev@fis.ucm.es

†Corresponding author: v.malyshev@rug.nl

¹It should be noticed that a thin layer of three-level V emitters also shows a similar behavior (see Refs. [69,70]).

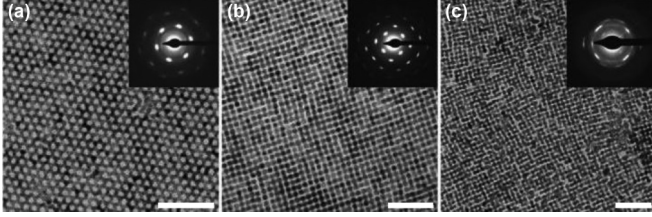


FIG. 1. PbSe rocksalt 2D nanostructures with (a) honeycomb and (b) square-lattice symmetry, (c) CdSe nanostructure with a compressed zinc-blende and slightly distorted square lattices (scale bars, 50 nm). Insets show the electrodiffraction patterns in the [111] (a) and [100] (b), (c) projections. The figure is from Ref. [7].

optical response has not been performed so far [23]. To uncover the character of the instabilities, we use the standard methods of nonlinear dynamics, such as the analysis of the Lyapunov exponents, bifurcation diagrams, phase space maps, and Fourier spectra [24–33]. Important technical results of our study are a simple parametric method of finding the exact solution of the nonlinear steady-state multilevel Maxwell-Bloch equations and a method of bifurcation diagram calculation that can be used for a wide class of systems.

The arrangement of the paper is as follows. In the next section, we describe the model of a 2D supercrystal comprised of SQDs and the mathematical formalism to treat its optical response. We use for that the one-particle density matrix formalism within the rotating wave approximation (RWA), where the total retarded dipole-dipole interactions between pointlike SQDs are taken into account. In Sec. III, the general formalism is simplified making use of the mean field approximation, and the mean field parameters (the collective energy-level shift and radiation damping) are calculated. In Sec. IV, we present the results of numerical calculations of the supercrystal optical response, including the steady-state solution (Sec. IV A), an analysis of bifurcations occurring in the system (Sec. IV B), and the system's dynamics (Sec. IV C) for two conditions of excitation: (i) the external field is tuned into the one-exciton transition and (ii) it is in resonance with the coherent two-photon transition (with the simultaneous absorption of two photons). A rationale for the physical mechanism of the effects found is provided in Sec. IV D. In Sec. V we show that the 2D SQD supercrystal can operate as a bistable nanoscale mirror. Section VI concludes the paper.

II. MODEL AND THEORETICAL BACKGROUND

We consider a 2D supercrystal comprising identical semiconductor quantum dots (SQDs). The optical excitations in an SQD are confined excitons. In such a system, the degeneracy of the one-exciton state is lifted due to the anisotropic electron-hole exchange, leading to two split linearly polarized one-exciton states (see, e.g., Refs. [34–36]). In this case, the ground state is coupled to the biexciton state via the linearly polarized one-exciton transitions. By choosing the appropriate polarization of the applied field, i.e., selecting one of the single-exciton states, the system effectively acquires a three-level ladderlike structure with a ground state $|1\rangle$, one exciton

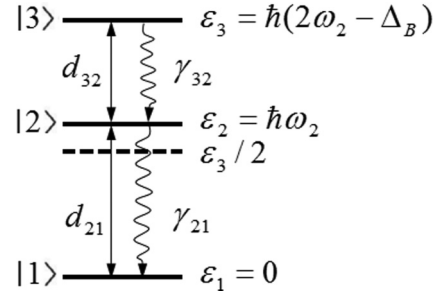


FIG. 2. Energy-level diagram of the ladder-type three-level SQD: $|1\rangle$, $|2\rangle$, and $|3\rangle$ are the ground, one-exciton, and biexciton states, respectively. The energies of corresponding states are $\varepsilon_1 = 0$, $\varepsilon_2 = \hbar\omega_2$, and $\varepsilon_3 = \hbar(2\omega_2 - \Delta_B)$, where, $\hbar\Delta_B$ is the biexciton binding energy. Allowed transitions with the corresponding transition dipole moments \mathbf{d}_{21} and \mathbf{d}_{32} are indicated by solid arrows. Wavy arrows denote the allowed spontaneous transitions with rates γ_{32} and γ_{21} . The dashed horizontal line shows the energy of the coherent two-photon resonance (the corresponding $1 \leftrightarrow 3$ transition occurs with the simultaneous absorption of two $\varepsilon_3/2$ photons).

state $|2\rangle$, and biexciton state $|3\rangle$ with corresponding energies $\varepsilon_1 = 0$, $\varepsilon_2 = \hbar\omega_2$, and $\varepsilon_3 = \hbar\omega_3 = \hbar(2\omega_2 - \Delta_B)$, where $\hbar\Delta_B$ is biexciton binding energy (see Fig. 2). Within this model, the allowed transitions, induced by the external field, are $|1\rangle \leftrightarrow |2\rangle$ and $|2\rangle \leftrightarrow |3\rangle$, which are characterized by the transition dipole moments \mathbf{d}_{21} and \mathbf{d}_{32} , respectively. For the sake of simplicity, we assume that they are real. The states $|3\rangle$ and $|2\rangle$ spontaneously decay with rates γ_{32} and γ_{21} , accordingly. Note that the biexciton state $|3\rangle$, having no allowed transition dipole moment from the ground state $|1\rangle$, can be populated either via consecutive $|1\rangle \rightarrow |2\rangle \rightarrow |3\rangle$ transitions or via the simultaneous absorption of two photons of frequency $\omega_3/2$. In what follows, we will consider both options.

The optical dynamics of SQDs is described by means of the Lindblad quantum master equation for the density operator $\rho(t)$ [37,38], which in the rotating frame (with the frequency ω_0 of the external field) reads as

$$\dot{\rho}(t) = -\frac{i}{\hbar}[H^{\text{RWA}}(t), \rho(t)] + \mathcal{L}\{\rho(t)\}, \quad (1a)$$

$$H^{\text{RWA}}(t) = \hbar \sum_{\mathbf{n}} (\Delta_{21}\sigma_{22}^{\mathbf{n}} + \Delta_{31}\sigma_{33}^{\mathbf{n}}) - i\hbar \sum_{\mathbf{n}} [\Omega_{21}^{\mathbf{n}}(t)\sigma_{21}^{\mathbf{n}} + \Omega_{32}^{\mathbf{n}}(t)\sigma_{32}^{\mathbf{n}}] + \text{H.c.}, \quad (1b)$$

$$\mathcal{L}\{\rho(t)\} = \frac{\gamma_{21}}{2} \sum_{\mathbf{n}} ([\sigma_{12}^{\mathbf{n}}\rho(t), \sigma_{21}^{\mathbf{n}}] + [\sigma_{12}^{\mathbf{n}}, \rho(t)\sigma_{21}^{\mathbf{n}}]) + \frac{\gamma_{32}}{2} \sum_{\mathbf{n}} ([\sigma_{23}^{\mathbf{n}}\rho(t), \sigma_{32}^{\mathbf{n}}] + [\sigma_{23}^{\mathbf{n}}, \rho(t)\sigma_{32}^{\mathbf{n}}]), \quad (1c)$$

$$\sigma_{ij}^{\mathbf{n}} = |\mathbf{n}i\rangle\langle\mathbf{n}j|, \quad i, j = 1, 2, 3. \quad (1d)$$

In Eq. (1a), \hbar is the reduced Planck constant, H^{RWA} is the SQD Hamiltonian in the RWA, $[A, B]$ denotes the commutator, \mathcal{L} is the Lindblad relaxation operator, given by Eq. (1c) [37,38]. In Eq. (1b), $\Delta_{21} = \omega_2 - \omega_0$ and $\Delta_{31} = \omega_3 - 2\omega_0$ are the energies of states $|2\rangle$ and $|3\rangle$ in the rotating frame, accordingly. Alternatively, these quantities can be interpreted as the detunings away from the one-photon resonance and the

coherent two-photon resonance, respectively. $\Omega_{21}^{\mathbf{n}}(t) = \mathbf{d}_{21} \mathbf{E}_{\mathbf{n}}(t)/\hbar$ and $\Omega_{32}^{\mathbf{n}}(t) = \mathbf{d}_{32} \mathbf{E}_{\mathbf{n}}(t)/\hbar$, where $\mathbf{E}_{\mathbf{n}}(t)$ is the slowly varying amplitude of the total field driving the optical transitions in the \mathbf{n} th SQD, $\mathcal{E}_{\mathbf{n}}(t) = \mathbf{E}_{\mathbf{n}}(t) \exp(-i\omega_0 t) + \text{c.c.}$. The latter is the sum of the applied field $\mathcal{E}_{\mathbf{n}}^0(t) = \mathbf{E}_{\mathbf{n}}^0(t) \exp(-i\omega_0 t) + \text{c.c.}$ and the field produced by all others SQDs in place of the \mathbf{n} th SQD, $\mathcal{E}_{\mathbf{n}}^{\text{loc}}(t) = \sum_{\mathbf{m}} \mathcal{E}_{\mathbf{mn}}(t) = \sum_{\mathbf{m}} \mathbf{E}_{\mathbf{mn}}(t) \exp(-i\omega_0 t) + \text{c.c.}$, where the amplitude $\mathbf{E}_{\mathbf{mn}}(t)$ is given by (see, e.g., Refs. [39,40])

$$\begin{aligned} \mathbf{E}_{\mathbf{mn}}(t) = & \left\{ \left[\frac{3}{r_{\mathbf{mn}}^3} - \frac{3ik_0}{r_{\mathbf{mn}}^2} - \frac{k_0^2}{r_{\mathbf{mn}}} \right] (\mathbf{d}_{21} \mathbf{u}_{\mathbf{mn}}) \mathbf{u}_{\mathbf{mn}} \right. \\ & - \left. \left[\frac{1}{r_{\mathbf{mn}}^3} - \frac{ik_0}{r_{\mathbf{mn}}^2} - \frac{k_0^2}{r_{\mathbf{mn}}} \right] \mathbf{d}_{21} \right\} \rho_{21}^{\mathbf{m}}(t') e^{ik_0 r_{\mathbf{mn}}} \\ & + \left\{ \left[\frac{3}{r_{\mathbf{mn}}^3} - \frac{3ik_0}{r_{\mathbf{mn}}^2} - \frac{k_0^2}{r_{\mathbf{mn}}} \right] (\mathbf{d}_{32} \mathbf{u}_{\mathbf{mn}}) \mathbf{u}_{\mathbf{mn}} \right. \\ & - \left. \left[\frac{1}{r_{\mathbf{mn}}^3} - \frac{ik_0}{r_{\mathbf{mn}}^2} - \frac{k_0^2}{r_{\mathbf{mn}}} \right] \mathbf{d}_{32} \right\} \rho_{32}^{\mathbf{m}}(t') e^{ik_0 r_{\mathbf{mn}}}, \quad (2) \end{aligned}$$

where $r_{\mathbf{mn}}$ is the distance between sites \mathbf{m} and \mathbf{n} , $k_0 = \omega_0/c$ (c is the speed of light in vacuum), $\mathbf{u}_{\mathbf{mn}} = \mathbf{r}_{\mathbf{mn}}/r_{\mathbf{mn}}$ is the unit vector along $\mathbf{r}_{\mathbf{mn}}$, and $t' = t - r_{\mathbf{mn}}/c$. Equation (2) represents the field (amplitude) produced by an oscillating dipole $\mathbf{d}_{21} R_{21}^{\mathbf{m}}(t') + \mathbf{d}_{32} R_{32}^{\mathbf{m}}(t')$ situated at a point $\mathbf{r}_{\mathbf{m}}$ in another point $\mathbf{r}_{\mathbf{n}}$ at an instant t , accounting for retardation: $t - t' = r_{\mathbf{mn}}/c$.² Using Eq. (2), the fields $\Omega_{\alpha\beta}^{\mathbf{n}}(t)$ ($\alpha\beta = 21, 32$) can be written in the form

$$\Omega_{\alpha\beta}^{\mathbf{n}}(t) = \Omega_{\alpha\beta}^{0\mathbf{n}}(t) + \sum_{\mathbf{m}} (\gamma_{\alpha\beta}^{\mathbf{mn}} + i\Delta_{\alpha\beta}^{\mathbf{mn}}) \rho_{\alpha\beta}^{\mathbf{m}}(t'), \quad (3a)$$

$$\begin{aligned} \gamma_{\alpha\beta}^{\mathbf{mn}} = & \frac{3\gamma_{\alpha\beta}}{4(k_0 a)^3} \left\{ \left[(k_0 a)^2 \frac{\kappa_{\alpha\beta}^{\mathbf{mn}}}{|\mathbf{m} - \mathbf{n}|} - \frac{\chi_{\alpha\beta}^{\mathbf{mn}}}{|\mathbf{m} - \mathbf{n}|^3} \right] \right. \\ & \times \sin(k_0 a |\mathbf{m} - \mathbf{n}|) + k_0 a \frac{\chi_{\alpha\beta}^{\mathbf{mn}}}{|\mathbf{m} - \mathbf{n}|^2} \cos(k_0 a |\mathbf{m} - \mathbf{n}|) \left. \right\}, \quad (3b) \end{aligned}$$

$$\begin{aligned} \Delta_{\alpha\beta}^{\mathbf{mn}} = & \frac{3\gamma_{\alpha\beta}}{4(k_0 a)^3} \left\{ \left[\frac{\chi_{\alpha\beta}^{\mathbf{mn}}}{|\mathbf{m} - \mathbf{n}|^3} - (k_0 a)^2 \frac{\kappa_{\alpha\beta}^{\mathbf{mn}}}{|\mathbf{m} - \mathbf{n}|} \right] \right. \\ & \times \cos(k_0 a |\mathbf{m} - \mathbf{n}|) + k_0 a \frac{\chi_{\alpha\beta}^{\mathbf{mn}}}{|\mathbf{m} - \mathbf{n}|^2} \sin(k_0 a |\mathbf{m} - \mathbf{n}|) \left. \right\}, \quad (3c) \end{aligned}$$

²Strictly speaking, this field should be the field acting *inside* the SQD; the latter differs from the field acting *on* the SQD by a screening factor which depends on the system geometry and material parameters. In the simplest case of a spherical dot in a homogeneous environment this factor can be obtained analytically (see, e.g., Ref. [73]). A realistic SQD array is a considerably more complicated system involving a nonhomogeneous host, at least three different materials, and a number of geometrical parameters. We believe that explicit calculation of the screening factors in this case would introduce unnecessary level of detail and obscure further analysis. Therefore, for the sake of simplicity, we consider a SQD as a pointlike system in a homogeneous host; all the fields entering the Lindblad equations should be interpreted as those rescaled by appropriate screening factors.

$$\kappa_{\alpha\beta}^{\mathbf{mn}} = 1 - (\mathbf{e}_{\alpha\beta} \mathbf{u}_{\mathbf{mn}})^2, \quad \chi_{\alpha\beta}^{\mathbf{mn}} = 1 - 3(\mathbf{e}_{\alpha\beta} \mathbf{u}_{\mathbf{mn}})^2. \quad (3d)$$

We used in Eqs. (3b) and (3c) the expression $\gamma_{\alpha\beta} = 4|\mathbf{d}_{\alpha\beta}|^2 \omega_{\alpha\beta}^3 / (3\hbar c^3)$. In Eq. (3d), $\mathbf{e}_{\alpha\beta} = \mathbf{d}_{\alpha\beta}/d_{\alpha\beta}$ is the unit vector along $\mathbf{d}_{\alpha\beta}$. The matrices $\gamma_{\alpha\beta}^{\mathbf{mn}}$ and $\Delta_{\alpha\beta}^{\mathbf{mn}}$ represent the real and imaginary parts of the retarded dipole-dipole interaction of \mathbf{n} th and \mathbf{m} th SQDs.

Equation (1a), written in the site basis $|\mathbf{n}i\rangle$ ($i = 1, 2, 3$), reads as

$$\dot{\rho}_{11}^{\mathbf{n}} = \gamma_{21} \rho_{22}^{\mathbf{n}} + \Omega_{21}^{\mathbf{n}} \rho_{21}^{\mathbf{n}*} + \Omega_{21}^{\mathbf{n}*} \rho_{21}^{\mathbf{n}}, \quad (4a)$$

$$\begin{aligned} \dot{\rho}_{22}^{\mathbf{n}} = & -\gamma_{21} \rho_{22}^{\mathbf{n}} + \gamma_{32} \rho_{33}^{\mathbf{n}} - \Omega_{21}^{\mathbf{n}} \rho_{21}^{\mathbf{n}*} - \Omega_{21}^{\mathbf{n}*} \rho_{21}^{\mathbf{n}} \\ & + \Omega_{32}^{\mathbf{n}} \rho_{32}^{\mathbf{n}*} + \Omega_{32}^{\mathbf{n}*} \rho_{32}^{\mathbf{n}}, \quad (4b) \end{aligned}$$

$$\dot{\rho}_{33}^{\mathbf{n}} = -\gamma_{32} \rho_{33}^{\mathbf{n}} - \Omega_{32}^{\mathbf{n}} \rho_{32}^{\mathbf{n}*} - \Omega_{32}^{\mathbf{n}*} \rho_{32}^{\mathbf{n}}, \quad (4c)$$

$$\dot{\rho}_{21}^{\mathbf{n}} = -(i\Delta_{21} + \frac{1}{2}\gamma_{21}) \rho_{21}^{\mathbf{n}} + \Omega_{21}^{\mathbf{n}} (\rho_{22}^{\mathbf{n}} - \rho_{11}^{\mathbf{n}}) + \Omega_{32}^{\mathbf{n}*} \rho_{31}, \quad (4d)$$

$$\begin{aligned} \dot{\rho}_{32}^{\mathbf{n}} = & -[i\Delta_{32} + \frac{1}{2}(\gamma_{32} + \gamma_{21})] \rho_{32}^{\mathbf{n}} \\ & + \Omega_{32}^{\mathbf{n}} (\rho_{33}^{\mathbf{n}} - \rho_{22}^{\mathbf{n}}) - \Omega_{21}^{\mathbf{n}*} \rho_{31}^{\mathbf{n}}, \quad (4e) \end{aligned}$$

$$\dot{\rho}_{31}^{\mathbf{n}} = -(i\Delta_{31} + \frac{1}{2}\gamma_{32}) \rho_{31}^{\mathbf{n}} - \Omega_{32}^{\mathbf{n}} \rho_{21}^{\mathbf{n}} + \Omega_{21}^{\mathbf{n}} \rho_{32}^{\mathbf{n}}, \quad (4f)$$

where $\Omega_{21}^{\mathbf{n}}$ and $\Omega_{32}^{\mathbf{n}}$ are given by Eqs. (3a)–(3d). The time dependence of all relevant quantities is dropped here.

It is worth to noting that Eqs. (4a)–(4f) represent a set of equations for the one-particle density matrix, where the quantum correlations of the dipole operators of different SQDs are neglected that implies that $\langle \hat{d}_{\mathbf{n}} \hat{d}_{\mathbf{m}} \rangle = \langle \hat{d}_{\mathbf{n}} \rangle \langle \hat{d}_{\mathbf{m}} \rangle$, where $\langle \dots \rangle$ denotes the quantum mechanical average. A proof of this assumption is a standalone problem to be solved, which is beyond the scope of this paper.

III. MEAN FIELD APPROXIMATION

The set of Eqs. (4a)–(4f) allows one to study the optical response of a SQD monolayer, without any limitation to the layer's size, lattice geometry, and the spatial profile of the external field amplitude $\mathbf{E}_0^{\mathbf{n}}$. Here, we restrict our consideration to a spatially homogeneous case, when all relevant quantities entering Eqs. (4a)–(4f) do not depend on the SQD's position \mathbf{n} . In fact, this approximation is equivalent to taking into account the Lorentz local field correction to the field acting on an emitter, which has been widely used when analyzing the optical response of dense bulk media, both linear [41,42] and nonlinear [13,16,22,43–45]. This approximation intuitively seems to be appropriate for an infinite layer, however, for a finite sample, its validity should be examined. Nevertheless, as we show below, even this simplest model predicts a variety of fascinating effects. We consider a simple square lattice of SQDs in order to avoid unnecessary computational complications.

Thus, we neglect the spatial dependence of all functions in Eqs. (4a)–(4f). Additionally, we assume for the sake of simplicity that the transition dipoles \mathbf{d}_{21} and \mathbf{d}_{32} are parallel to each other, $\mathbf{d}_{32} = \mu \mathbf{d}_{21} \equiv \mu \mathbf{d}$ (not a principal limitation). Accordingly, $\gamma_{32} = \mu^2 \gamma_{21} \equiv \mu^2 \gamma$ and $\Omega_{32} = \mu \Omega_{21} \equiv \mu \Omega$. Then, the system of equations (4a)–(4f) takes

the form³

$$\dot{\rho}_{11} = \gamma \rho_{22} + \Omega \rho_{21}^* + \Omega^* \rho_{21}, \quad (5a)$$

$$\dot{\rho}_{22} = -\gamma \rho_{22} + \mu^2 \gamma \rho_{33} - \Omega \rho_{21}^* - \Omega^* \rho_{21} + \mu(\Omega \rho_{32}^* + \Omega^* \rho_{32}), \quad (5b)$$

$$\dot{\rho}_{33} = -\mu^2 \gamma \rho_{33} - \mu(\Omega \rho_{32}^* + \Omega^* \rho_{32}), \quad (5c)$$

$$\dot{\rho}_{21} = -(i\Delta_{21} + \frac{1}{2}\gamma)\rho_{21} + \Omega(\rho_{22} - \rho_{11}) + \mu\Omega^* \rho_{31}, \quad (5d)$$

$$\dot{\rho}_{32} = -[i\Delta_{32} + \frac{1}{2}(1 + \mu^2)\gamma]\rho_{32} + \mu\Omega(\rho_{33} - \rho_{22}) - \Omega^* \rho_{31}, \quad (5e)$$

$$\dot{\rho}_{31} = -(i\Delta_{31} + \frac{1}{2}\mu^2\gamma)\rho_{31} - \mu\Omega\rho_{21} + \Omega\rho_{32}, \quad (5f)$$

$$\Omega = \Omega_0 + (\gamma_R + i\Delta_L)(\rho_{21} + \mu\rho_{32}), \quad (5g)$$

where the constants γ_R and Δ_L are given by

$$\gamma_R = \sum_{\mathbf{m}(\neq\mathbf{n})} \gamma_{21}^{\mathbf{mn}} = \frac{3\gamma}{4(k_0a)^3} \sum_{\mathbf{n}(\neq\mathbf{0})} \left\{ \left[(k_0a)^2 \frac{\kappa_{\mathbf{n}}}{|\mathbf{n}|} - \frac{\chi_{\mathbf{n}}}{|\mathbf{n}|^3} \right] \times \sin(k_0a|\mathbf{n}|) + k_0a \frac{\chi_{\mathbf{n}}}{|\mathbf{n}|^2} \cos(k_0a|\mathbf{n}|) \right\}, \quad (6a)$$

$$\Delta_L = \sum_{\mathbf{m}(\neq\mathbf{n})} \Delta_{21}^{\mathbf{mn}} = \frac{3\gamma}{4(k_0a)^3} \sum_{\mathbf{n}(\neq\mathbf{0})} \left\{ \left[\frac{\chi_{\mathbf{n}}}{|\mathbf{n}|^3} - (k_0a)^2 \frac{\kappa_{\mathbf{n}}}{|\mathbf{n}|} \right] \times \cos(k_0a|\mathbf{n}|) + k_0a \frac{\chi_{\mathbf{n}}}{|\mathbf{n}|^2} \sin(k_0a|\mathbf{n}|) \right\}, \quad (6b)$$

$$\kappa_{\mathbf{n}} = 1 - (\mathbf{e}\mathbf{u}_{\mathbf{n}})^2, \quad \chi_{\mathbf{n}} = 1 - 3(\mathbf{e}\mathbf{u}_{\mathbf{n}})^2. \quad (6c)$$

Recall that the summation in Eqs. (6a) and (6b) runs over sites $\mathbf{n} = (n_x, n_y)$ of a simple square lattice, where $n_x = 0, \pm 1, \pm 2, \pm 3 \dots \pm N_x$, $n_y = 0, \pm 1, \pm 2, \pm 3 \dots \pm N_y$, and $\mathbf{e} = \mathbf{d}/d$ is the unit vector along the transition dipole moment \mathbf{d}_{21} .

Next, we are interested in (k_0a) scaling of the constants γ_R and Δ_L . First, consider a pointlike system, when the lateral lattice sizes $N_x a$ and $N_y a$ are much smaller than the reduced wavelength $\tilde{\lambda} = k_0^{-1}$. Then, making the expansion of sine and cosine functions in Eqs. (6a) and (6b) to the lowest order with respect to $k_0a \ll 1$, one finds

$$\gamma_R = \frac{3\gamma}{4} \sum_{\mathbf{n}(\neq\mathbf{0})} \kappa_{\mathbf{n}} = \frac{3}{8} \gamma N, \quad (7a)$$

$$\Delta_L = \frac{3\gamma}{4(k_0a)^3} \sum_{\mathbf{n}(\neq\mathbf{0})} \frac{\chi_{\mathbf{n}}}{|\mathbf{n}|^3} = -\frac{3\gamma}{2(k_0a)^3} \zeta(3/2)\beta(3/2) \simeq -3.39 \frac{\gamma}{(k_0a)^3} = -3.39\gamma \left(\frac{\tilde{\lambda}}{a}\right)^3, \quad (7b)$$

where $N = 4N_x N_y$ is the total number of sites in the lattice, $\zeta(x)$ is the Riman z function, and $\beta(x) = \sum_{n=0}^{\infty} (-1)^n (2n+1)^{-x}$ is the analytical continuation of the Dirichlet series [46]. When deriving Eq. (7a) we used the fact that $\sum_{\mathbf{n}(\neq\mathbf{0})} \kappa_{\mathbf{n}} = N/2$.

³Note that Eqs. (5a)–(5g) are algebraically equivalent to the equations for a heterodimer comprising a metallic nanoparticle and a semiconductor quantum dot subjected to a quasiresonant irradiation (see Refs. [63,74]).

Furthermore, the formula (7b) follows from Eq. (A20) of Ref. [47] at $\theta = \pi/2$. As is seen from Eq. (7a), γ_R does not depend on k_0a ; it is determined by the total number of SQDs in the lattice and describes the collective (Dicke) radiative relaxation of SQDs as all the SQD's dipoles are in phase for a pointlike system [39,40,48]. Oppositely, Δ_L shows (k_0a) scaling, corresponding to the near-zone dipole-dipole interaction of a given SQD with all others.

For a large system ($N_x a, N_y a \gg \tilde{\lambda}$), one has to use Eqs. (6a) and (6b) to calculate γ_R and Δ_L , keeping all terms when performing summation. It turns out that the sums in Eqs. (7a) and (7b), which contain summands proportional to $|\mathbf{n}|^{-1}$, converge very slowly as the lattice size increases, which results in diminishing oscillations of γ_R and Δ_L around their asymptotic values given by (see Appendix A)

$$\gamma_R \simeq 4.51 \frac{\gamma}{(k_0a)^2} = 4.51\gamma \left(\frac{\tilde{\lambda}}{a}\right)^2, \quad (8a)$$

$$\Delta_L \simeq -3.35 \frac{\gamma}{(k_0a)^3} = -3.35\gamma \left(\frac{\tilde{\lambda}}{a}\right)^3. \quad (8b)$$

As follows from Eq. (8a), for a large system, the collective radiation rate γ_R is determined by a number of SQDs within an area on the order of $\tilde{\lambda}^2$: all SQD's dipoles are in phase there. Recall that for a linear chain of emitters, $\gamma_R \sim \tilde{\lambda}/a$ [39]. On the contrary, the near-zone dipole-dipole interaction Δ_L changes insignificantly compared with that for a pointlike system [compare Eq. (8b) with (7b)].

It should be noticed that irrespectively of the system size, the inequality $|\Delta_L| \gg \gamma_R$ is always fulfilled for a dense system, $\tilde{\lambda} \gg a$. We will use this relationship in our analysis of the supercrystal's optical response.

IV. NUMERICS

We performed calculations of the system dynamics for two resonance conditions: (i) the applied field Ω_0 is in resonance with the one-exciton transition $\omega_0 = \omega_2$ ($\Delta_{21} = 0, \Delta_{32} = -\Delta_B$) of a single emitter (conventionally called in what follows as one-photon resonance) and (ii) it is tuned to the two-photon resonance $\omega_0 = \omega_3/2$ ($\Delta_{21} = \Delta_B/2, \Delta_{32} = -\Delta_B/2$). In reality, however, the single-emitter resonance $\Delta_{21} = 0$ is redshifted due to the near-zone SQD-SQD interactions by $|\Delta_L|$, so that the resonance in the linear low-field intensity regime is defined by the condition $\Delta_{21} = |\Delta_L|$ (see Sec. IV D for detail).

In our numerical calculations we use the typical values of optical parameters of the SQDs (emitting in the visible) and SQD supercrystals (see, e.g., Fig. 1). More specifically, the spontaneous decay rate $\gamma \approx 3 \times 10^9 \text{ s}^{-1}$ and the ratio $\mu = d_{32}/d_{21} = \sqrt{\gamma_{32}/\gamma_{21}} = \sqrt{2/3}$. The magnitudes of γ_R and Δ_L depend on the ratio $\tilde{\lambda}/a$. Taking $\tilde{\lambda} \sim 100\text{--}200 \text{ nm}$ and $a \sim 10\text{--}20 \text{ nm}$, one obtains the following estimates for these two constants: $\gamma_R \sim 10^{12} \text{ s}^{-1}$ and $|\Delta_L| \sim 10^{13} \text{ s}^{-1}$. The typical values of the biexciton binding energy Δ_B are on the order of several meV, $\Delta_B \sim 2.5\text{--}10 \text{ meV} \sim 10^{12} \text{ s}^{-1}$, although for some 2D systems, like transition metal dichalcogenides [49,50], it can be one order of magnitude larger. Therefore, the biexciton binding energy $\hbar\Delta_B$ is considered as a variable parameter. In what follows, the spontaneous emission rate γ

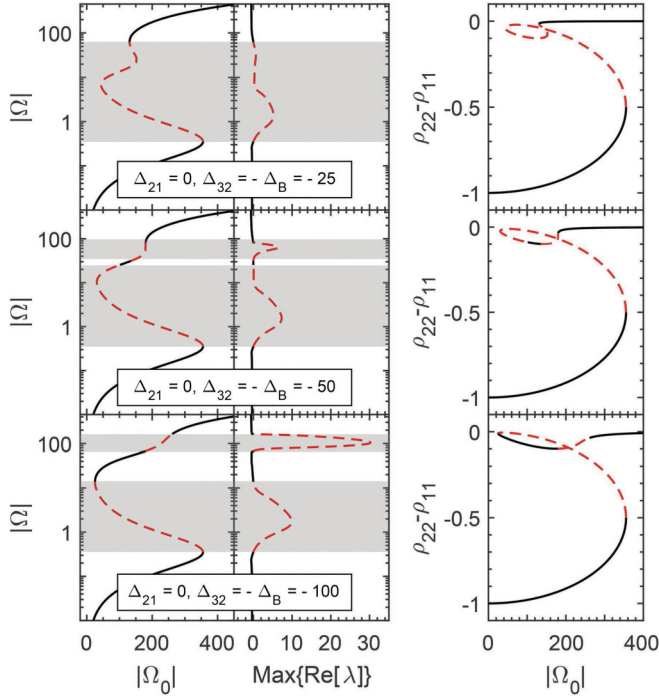


FIG. 3. Steady-state solutions to Eqs. (5a)–(5g) for the case of one-photon resonance ($\Delta_{21} = 0$, $\Delta_{32} = -\Delta_B$) and for different values of the biexciton binding energy Δ_B (shown in the plots). The left column shows dependencies of the total field magnitude $|\Omega|$ on the excitation field $|\Omega_0|$, right column dependencies of the population difference $\rho_{22} - \rho_{11}$ on the $|\Omega_0|$. Unstable regions of the stationary solutions are indicated by gray shading; the maximum values of the real parts of Lyapunov exponents $\max_k \text{Re}\lambda_k$ are shown in the middle column (see text for details). All frequency-dimension quantities are given in units of γ .

is used as the unit of all frequency-dimensional quantities, whereas γ^{-1} as the time unit. According to our estimates, we set in $\gamma_R = 100\gamma$ and $|\Delta_L| = 1000\gamma$.

Equations (5a)–(5g) belong to a class of so-called stiff differential equations, characterized by several significantly different timescales. In our case, these are defined by $\gamma^{-1} \gg \gamma_R^{-1} \gg |\Delta_L|^{-1}$. We therefore use specialized integration routines adapted for systems of such stiff equations, in particular, the ODE23tb of MATLAB and some implementations of methods based on the backward differentiation formulas.

A. Steady-state analysis

As the first step of studying the system optical response, we turn to the steady-state regime. By setting the time derivatives in Eqs. (5a)–(5g) to zero, we obtain the system of stationary nonlinear equations which we solve by our exact parametric method (detailed in Appendix B). The results for different values of the biexciton binding energy Δ_B are presented below in the series of figures.

Figures 3 and 4 show the dependence of the total field magnitude $|\Omega|$ (leftmost column) and the population difference $Z_{21} = \rho_{22} - \rho_{11}$ (rightmost column) on the external field magnitude $|\Omega_0|$ calculated for the one-photon ($\omega_0 = \omega_2$, $\Delta_{21} = 0$, $\Delta_{32} = -\Delta_B$) and two-photon ($\omega_0 = \omega_3/2$, $\Delta_{21} = -\Delta_{32} = \Delta_B/2$) resonance, respectively. As is seen from the figures,

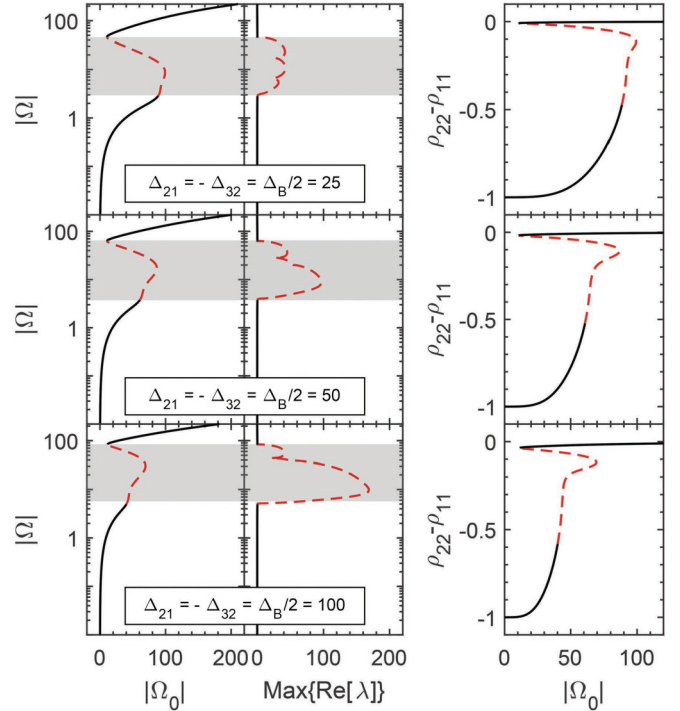


FIG. 4. Same as in Fig. 3, but for the case of the two-photon resonance ($\Delta_{21} = -\Delta_{32} = \Delta_B/2$).

the total field magnitude $|\Omega|$ can have several solutions (up to five for $\Delta_{32} = -50$) for a given value of the external field magnitude $|\Omega_0|$, which can give rise to multistability and hysteresis phenomenon (see Sec. IV C 3). We analyzed the stability of different branches by the standard Lyapunov exponents analysis [25,31]. To this end, we calculated the eigenvalues λ_k ($k = 1 \dots 8$) of the Jacobian matrix of the right-hand side of Eqs. (5a)–(5g) as a function of $|\Omega|$. The exponent with the maximal real part, $\max_k \text{Re}\lambda_k$, determines the stability of the steady-state solution: if $\max_k \text{Re}\lambda_k \leq 0$, the solution is stable and unstable otherwise. The values of $\max_k \text{Re}\lambda_k$ are plotted in the middle panels of Figs. 3 and 4. The shaded regions show the unstable parts of the steady-state solutions (with $\max_k \text{Re}\lambda_k > 0$).

We stress that not only the branches with the negative slope are unstable, which is always the case, but some parts of the branches with the positive slopes as well. This occurs for both the one- and two-photon resonance conditions. Quite remarkably, in the case of the one-photon resonance with $\Delta_B = 100$, a part of the upper branch of the steady-state solution is unstable. Moreover, for $\Delta_B = 50$, two unstable regions of the upper branch are separated by a stable one. The nature of these instabilities is discussed in Secs. IV B and IV C.

B. Bifurcation diagram

The bifurcation diagram is a very useful tool providing an insight into possible scenarios of the system behavior in a graphical way [26,27,29,32] by portraying the system dynamics qualitatively as a function of a control (bifurcation) parameter. In order to construct the bifurcation diagram, we address the dynamics of the total field magnitude $|\Omega(t)|$ (which is one of the possible measurable outputs) as a function

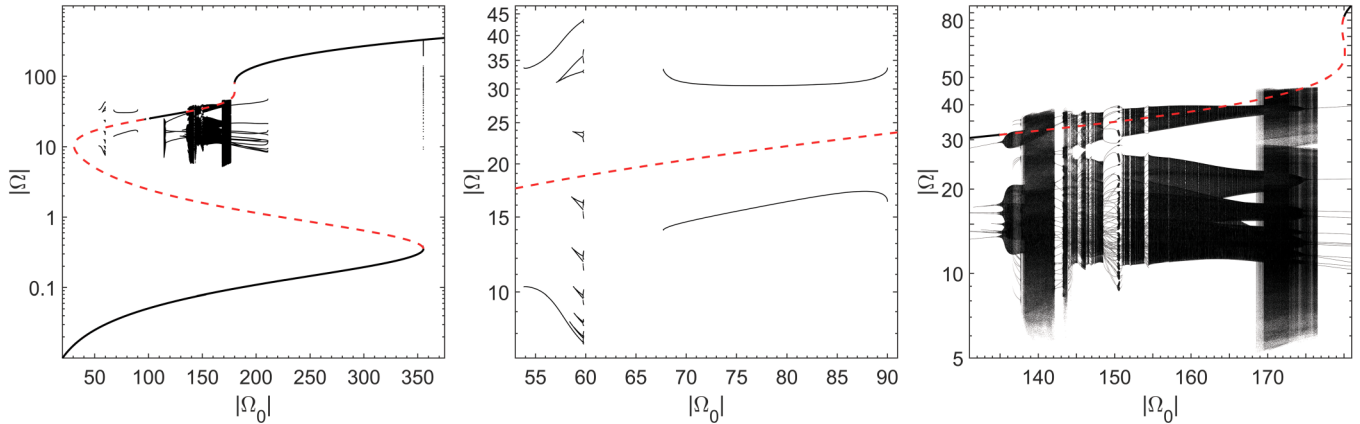


FIG. 5. Left panel: the overall bifurcation diagram [extrema of the total field magnitude $|\Omega(t)|$ on attractors as a function of the external field magnitude $|\Omega_0|$] calculated for the case of one-photon resonance $\Delta_{21} = 0$, $\Delta_{32} = -\Delta_B = -50$ (see text for details of the calculation method). Dashed red line shows the unstable part of the steady-state solution from Fig. 3, which is given for reference. Middle and right panels: blowups of the regions of the bifurcation diagram with nontrivial dynamics (see also Sec. IV C). All quantities are given in units of γ .

of the external field magnitude $|\Omega_0|$, which is the most natural bifurcation parameter for the system under consideration. To this end, for each $|\Omega_0|$ we plot a set of characteristic points of $|\Omega(t)|$, namely, all the extrema of the latter on an attractor.

Our proposed method of bifurcation diagram calculation is as follows. First, we note that the steady-state characteristics ($|\Omega|$ vs $|\Omega_0|$ dependence in Figs. 3 and 4) are multivalued, which can complicate numerical procedures considerably if the external field amplitude Ω_0 is swept. Therefore, we sweep the total field amplitude Ω instead. As we argue in Appendix B, the latter can be considered to be real without loss of generality [if appropriate phase transformations are performed, see Eq. (B3b)]. Thus, for each real valued Ω , we use Eq. (5g) to obtain the unique stationary (complex valued) Ω_0 , whose *absolute value* is used as the external field amplitude in Eqs. (5a)–(5g) to calculate the system dynamics. After going through a transient phase, the dynamics converges to an attractor. Then, we obtain all the extrema of the absolute value of the total field amplitude $|\Omega(t)|$ on the trajectory over a sufficiently long time interval. All such extrema are plotted as points for the current value of $|\Omega_0|$, forming the bifurcation diagram.

The distribution of the extrema provides qualitative information on possible types of the system dynamics. For example, if the dynamics converges to a stable fixed point, all the extrema collapse onto a single point (within the precision of the numerical method). The point coincides with the stable stationary value of the field (the extrema exist because the solution is typically still oscillating about the stationary value due to finite precision of numerical methods). If the dynamics converges to a periodic orbit, all the extrema collapse onto a finite set of points separated by gaps (see Fig. 5, middle panel). Quasiperiodic oscillations can turn up as vertical bars separated by gaps (see Fig. 5, right panel), while chaos would probably display itself as a continuous vertical line. The proposed representation of the system dynamics is somewhat similar to the Lorenz map [51] (in the sense that it uses extrema), but it contains considerably more information. On the other hand, it is also resembling the Poincaré map [25] (in the way it represents different types of dynamics), but it is less

complicated to calculate than the latter while providing almost equivalent qualitative information. We believe therefore that the proposed method of bifurcation diagram calculation is quite advantageous.

The choice of the initial conditions becomes very important when scanning for attractors with nontrivial dynamics (those different from a stable fixed point). Ideally, one should try out all possible initial conditions for each value of the bifurcation parameter, which is hardly feasible. Hereafter, we assume that the system can manifest interesting dynamics when it is “not too far” in the phase space from the unstable branches of the steady-state characteristics; we therefore use the following procedure to choose the initial conditions. At each step, i.e., for each value of $|\Omega|$, we are inspecting the solution from the previous step. If the previous solution appears to be on a nontrivial attractor, we take the previous solution at the final time instant as the initial condition for the current step. Thus, we try to keep the system in the basin of attraction of the nontrivial attractor. Otherwise, if the system is converging to a stable fixed point at the previous step, we take the steady-state solution corresponding to the current value of $|\Omega|$ as the initial condition. Such a solution can be on an unstable part of the stationary curve and yield some interesting dynamics. Besides, we are sweeping the parameter $|\Omega|$ across the window of interest back and forth, intending to discover the most complete set of attractors.

Finally, to ascertain that the dynamics has converged to an attractor, in other words, to make sure that the transient phase of the dynamics has passed, we apply the following procedure. We integrate the system over consecutive time intervals ΔT and calculate the range R_n of the function $|\Omega(t)|$ at each interval, i.e.,

$$R_n = \max_{\Delta T} |\Omega(t)| - \min_{\Delta T} |\Omega(t)|,$$

where n is the step number. The dynamics is considered to converge to an attractor when the range R_n stops growing and its change from one step to the next becomes sufficiently small in the following sense: $|R_{n+1} - R_n| < \epsilon_a$ and

$|R_{n+1} - R_n|/R_n < \epsilon_r$.⁴ In any case, the integration was stopped when the integration time reached T_{\max} . Unfortunately, we can not propose any general method to estimate the parameters ΔT , ϵ_a , ϵ_r , and T_{\max} . To determine their appropriate values, we analyzed the system dynamics on different types of attractors and found out that the set $\Delta T = 50$, $\epsilon_a = 0.001$, $\epsilon_r = 0.001$, and $T_{\max} = 10^4$ was working well in all cases we considered. Finally, when the dynamics converges to an attractor, the extrema of $|\Omega(t)|$ are calculated on the last time interval; their values are used to construct the bifurcation diagram as explained above.

Figure 5 presents the bifurcation diagram calculated for the case of the one-photon resonance $\Delta_{21} = 0$, $\Delta_{32} = -\Delta_B$, and the biexciton binding energy $\Delta_B = 50$. The steady-state characteristics from Fig. 3 is also plotted; the stable stationary branches (black lines) form the trivial part of the bifurcation diagram, while the unstable branches (red dashed line) are given for reference. The middle and right panels of the figure show blowups of the parts of the diagram with nontrivial dynamics. As expected, these parts are located in proximity to the unstable branches of the steady state. The figure shows that, although there are stable stationary solutions for all values of the external field magnitude $|\Omega_0|$, the system dynamics can be highly nontrivial, manifesting a wide range of attractor types. In particular, fingerprints of stable fixed points, periodic and aperiodic orbits, and chaotic trajectories can be seen.

As observed from Fig. 5, the system undergoes multiple bifurcations. Consider, for example, the bifurcation of limit cycles existing within the range of the external field magnitude $67 \lesssim |\Omega_0| \lesssim 90$ (middle panel of Fig. 5). When $|\Omega_0|$ crosses the left boundary of the interval, being swept down, the limit cycle disappears and the system is attracted to a stable fixed point which resides in the lower stable branch of the steady-state characteristics. This scenario resembles a subcritical Andronov-Hopf bifurcation [26,29,32]. Once at the stable branch, the system remains at this trivial attractor even if the field magnitude is swept up to fall again within the interval, where self-oscillations can exist. Here, we deal with hysteresis of the bifurcation diagram.

We turn now to the case when the system is in a stable fixed point belonging to the intermediate positive-slope branch of the steady-state characteristics, surrounded by the unstable parts, i.e., within the interval $100 \lesssim |\Omega_0| \lesssim 135$ (see the panel of Fig. 3 for $\Delta_B = 50$ and the right panel of Fig. 5). If the external field magnitude $|\Omega_0|$ starts to increase and crosses the right boundary of the interval, a limit cycle is created from a stable fixed point at $|\Omega_0| \approx 137$. This change of the character of dynamics resembles a supercritical Andronov-Hopf bifurcation [26,29,32]. Further, if the external field magnitude is swept back (starts to decrease), the system would follow the nontrivial attractor until its lower field extreme (at $|\Omega_0| \approx 115$), where the auto-oscillation disappears, and the system is attracted back to the stable fixed point at the upper steady-state branch.

⁴Additionally, one can apply the same criteria to the average $A_n = [\min_{\Delta T} |\Omega(t)| + \max_{\Delta T} |\Omega(t)|]/2$ to account for and get rid of the drift of the average toward an attractor.

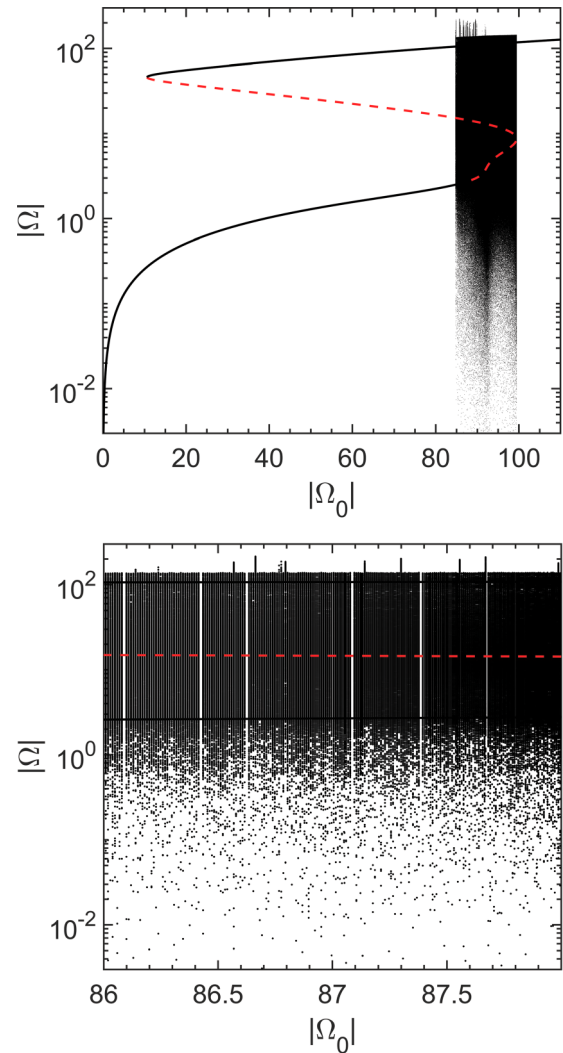


FIG. 6. Same as in Fig. 5 but for the case of two-photon resonance ($\Delta_{21} = -\Delta_{32} = \Delta_B/2$) with $\Delta_B = 50$. Upper panel: the overall diagram; lower panel: a blowup of a fragment of the above diagram showing its fine structure.

Figure 6 shows the extrema diagram calculated for the case of the two-photon resonance ($\Delta_{21} = -\Delta_{32} = \Delta_B/2 = 25$). The black vertical feature at $85 \lesssim |\Omega_0| \lesssim 100$ represents the most interesting part of the diagram with nontrivial dynamics. The feature consists of very densely packed points forming practically continuous vertical lines, which indicates that the extrema of the total field magnitude $|\Omega(t)|$ might be distributed randomly and that the signal is presumably of a chaotic nature. We confirmed the latter by calculating the Lyapunov spectra using the standard method based on the QR factorization (decomposition of a matrix into a product of an orthogonal matrix Q and an upper triangular one R) [52–58] and found that a typical spectrum contains one positive exponent, a zero one, and negative remaining exponents. The latter (+, 0, −, . . . , −) pattern of the signs of Lyapunov exponents is known to be a fingerprint of a chaotic trajectory. The typical value of the corresponding Lyapunov dimension, estimated using the Kaplan and Yorke’s conjecture [59,60], is $d_L \geq 4$.

However, this chaos may turn up to be transient, in the sense that, if the system is let to evolve for sufficiently long

time, it will finally be attracted to one of the stable steady-state points. Such events can be seen in the blowup shown in the lower panel of Fig. 6: the white gaps in the feature correspond to solutions that converged toward the stable stationary curve for $t \leq T_{\max}$. Our calculations showed that the time during which the transient chaotic dynamics exists is hardly predictable, besides this time seems to be very sensitive to initial conditions and the integration method, which is a typical feature of a transient chaos (see Refs. [61,62] and references therein).

Regarding bifurcations occurring in the present case, we can state with definiteness only about those which arise at the edges of the black feature: at the left edge, a stable fixed point loses its stability and bifurcates into a chaotic trajectory, while at the right one, the back bifurcation takes place.

Thus, the system dynamics can be very complex demonstrating a large variety of attractor types and bifurcations, some of which can manifest hysteresis. A detailed study of all possible bifurcations goes far beyond the scope of this paper; in what follows, we restrict ourselves to addressing some of the most prominent system dynamics scenarios in more detail.

C. Time-domain analysis

In this section, we present and discuss system dynamics on a variety of nontrivial attractors for either the one-photon ($\omega = \omega_2$) or two-photon ($\omega = \omega_3/2$) resonant excitation. We solve Eqs. (5a)–(5g) for two types of initial conditions: the system is initially in the ground state ($\rho_{11} = 1$, while all other density matrix elements are equal to zero) or in a given steady-state⁵ corresponding to the external field magnitude $|\Omega_0|$.

1. One-photon resonance ($\Delta_{21} = 0$, $\Delta_{32} = -\Delta_B$)

Figure 7 shows the results of time-domain calculations performed for the case of the one-photon resonance ($\Delta_{21} = 0$) with $\Delta_{32} = -\Delta_B = -50$. Three points on the unstable parts of the steady-state solution were used as initial conditions: ($|\Omega_0| = 68.1$, $|\Omega| = 20.1257$) (upper row), ($|\Omega_0| = 136$, $|\Omega| = 31.4674$) (middle row), and ($|\Omega_0| = 170$, $|\Omega| = 42.3836$) (bottom row).

The left panels in Fig. 7 show the time evolution of the total field magnitude $|\Omega|$. As is seen, after some delay which correlates well with the values of inverse Lyapunov exponents for the corresponding points of the steady-state solution (see Fig. 3, the middle panel for $\Delta_B = 50$) an instability starts to develop. At longer times, the latter acquires a sustained form, indicating that the system is on an attractor. In the middle panels, the Fourier spectra [$|\int dt \exp(i\omega t)\Omega(t)|$] on the attractor are plotted. The right panels show the trajectories on attractors in the reduced phase space ($\text{Re } \Omega$, $\text{Im } \Omega$).

The figure shows that the character of motion on the attractor depends on the initial point. For example, for ($|\Omega_0| =$

68.1, $|\Omega| = 20.1257$) (the upper row in Fig. 7), the system dynamics looks like a simple self-oscillation [see the left panel and also the inset for a blowup of the dynamics of $|\Omega(t)|$]. Accordingly, the Fourier spectrum (middle panel) contains a few well-defined harmonics of the base frequency while the phase space map (right panel) represents a closed curve, commonly called a limit cycle [25,31]. The pattern of the Lyapunov exponents signs ($0, -, \dots, -$) is also typical for a limit cycle.

For ($|\Omega_0| = 136$, $|\Omega| = 31.4674$) (the middle row in Fig. 7), the dynamics manifests signature of aperiodic oscillations. In this case the Fourier spectrum is also discrete, but now together with the equidistant peaks there are also satellites with incommensurate frequencies. The phase-space map represents a stripelike trajectory, densely filling a finite area in the phase space. This is a signature of aperiodic motion on a hypertorus.

Finally, for ($|\Omega_0| = 170$, $|\Omega| = 42.3836$) (the bottom row), the dynamics is more complicated (see the inset in the left panel). The Fourier spectrum consists of a set of broadened peaks at a noisy background (see also the inset in the middle panel). This regime is chaotic; our calculations of the Lyapunov exponents spectrum confirm that the signs of the exponents have the typical ($+, 0, -, \dots, -$) pattern and the Lyapunov dimension is $d_L \approx 3.42$.

2. Two-photon resonance ($\Delta_{21} = -\Delta_{32} = \Delta_B/2$)

In the case of the two-photon resonance ($\omega_0 = \omega_3/2$), a part of the lower branch of the steady-state solution with a positive slope is unstable (see Fig. 4). As a result, the dynamics can be nontrivial even if the system is initially in the ground state, in contrast to the case of the one-photon resonance discussed in the preceding section. We therefore consider both the steady-state and the ground-state initial conditions; the corresponding results are presented in Fig. 8.

The top row in Fig. 8 shows the system dynamics for $\Delta_B = 50$ and the steady-state initial condition at ($|\Omega_0| = 95$, $|\Omega| = 5.5$). As is seen, after a short transient phase, the system evolves toward the fixed point on the upper stable branch of the stationary curve that corresponds to $|\Omega_0| = 95$. Accordingly, the Fourier spectrum on the attractor consists of a single peak at zero frequency and the phase-space map is a point.

On the contrary, if the ground-state initial condition is used for the same external field magnitude $|\Omega_0| = 95$ (middle row), the dynamics is seemingly chaotic, manifesting a very irregular train of pulses. The Fourier spectrum is practically continuous in this case, while the reduced phase-space map of the trajectory seems to have a completely filled volume. The sign pattern of the Lyapunov exponents is ($+, 0, -, \dots, -$) indicating that the trajectory is indeed chaotic; the Lyapunov dimension is $d_L \approx 4.7$.

The results of calculations, performed for another value of the external field magnitude $|\Omega_0| = 95.2$, turned out to be essentially independent on the initial conditions. The output for the unstable steady-state point ($|\Omega_0| = 95.2$, $|\Omega| = 5.6$) is shown in the bottom row of Fig. 8 and reveals a chaotic behavior of the system, in contrast with the unstable steady-state point ($|\Omega_0| = 95$, $|\Omega| = 5.5$).

⁵When the system is exactly in a stationary state it remains there forever. However, due to the finite precision of numerical methods and the initial state itself, the system is in very small vicinity of the exact stationary state. Therefore, it is either attracted to the steady state (if it is a stable fixed point) or drifts away from it if the stationary state is unstable.

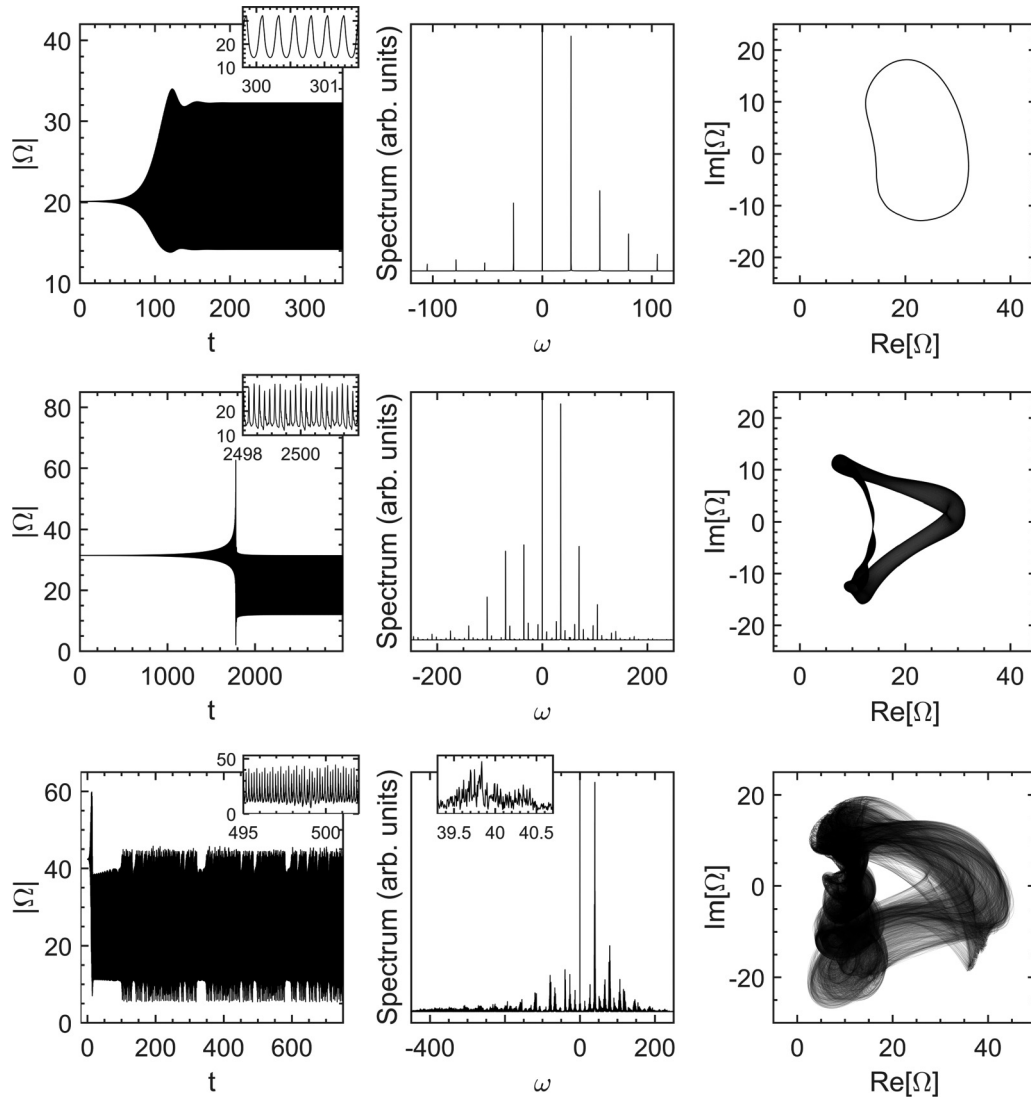


FIG. 7. The dynamics of the total field magnitude $|\Omega(t)|$ (left column, insets show blowups of the dynamics), the Fourier spectrum (middle column), and two-dimensional map of $(\text{Re}[\Omega], \text{Im}[\Omega])$ on the attractor (right column). The results are calculated for the case of the one-photon resonance ($\Delta_{21} = 0, \Delta_{32} = -\Delta_B$) with $\Delta_B = 50$. The initial conditions were taken to be on the steady-state characteristics at $(|\Omega_0| = 68.1, |\Omega| = 20.1257)$ (upper row), $(|\Omega_0| = 136, |\Omega| = 31.4674)$ (middle row), and $(|\Omega_0| = 170, |\Omega| = 42.3836)$ (bottom row). All frequency-dimension quantities are given in units of γ , while time is in units of γ^{-1} .

3. Optical hysteresis

The multivalued character of the steady state (see Figs. 3 and 4) can give rise to a hysteresis of the system response, when the external field magnitude $|\Omega_0|$ is slowly swept back and forth. It is unclear, however, whether the hysteresis loops are stable because some parts of the steady-state solutions, through which the system is driven by the field, are unstable. Figures 9 and 10 show the corresponding results for the one- and two-photon resonance excitation, respectively. In both cases, the hysteresis loops appear to be stable.

In the hysteresis loop calculations, the external field magnitude $|\Omega_0|$ was swept linearly in the following way: $|\Omega_0| = 0.002t$ for $0 \leq t \leq T$ and $|\Omega_0| = 0.002(2T - t)$ for $T \leq t \leq 2T$, where the time T is chosen in such a way that the whole multivalued part of the steady-state characteristics is scanned.

From Figs. 9 and 10 it follows that in both cases, the optical response is bistable within a window of external field amplitudes. As the external field magnitude $|\Omega_0|$ is increased from zero, the total field magnitude $|\Omega|$ follows the lower branch of the steady-state characteristics until it reaches the right critical point at which $|\Omega|$ abruptly jumps up to the upper stable branch where the system is saturated. On decreasing $|\Omega_0|$ the system remains on the upper branch until $|\Omega_0|$ reaches the left critical point, where the system abruptly jumps down to the lower branch, completing the hysteresis loop. Branches with the negative slope are not accessible in the adiabatic numerical experiment.

D. Discussion

As we argue above, the considered system demonstrates a very rich optical dynamics: multistability, periodic and

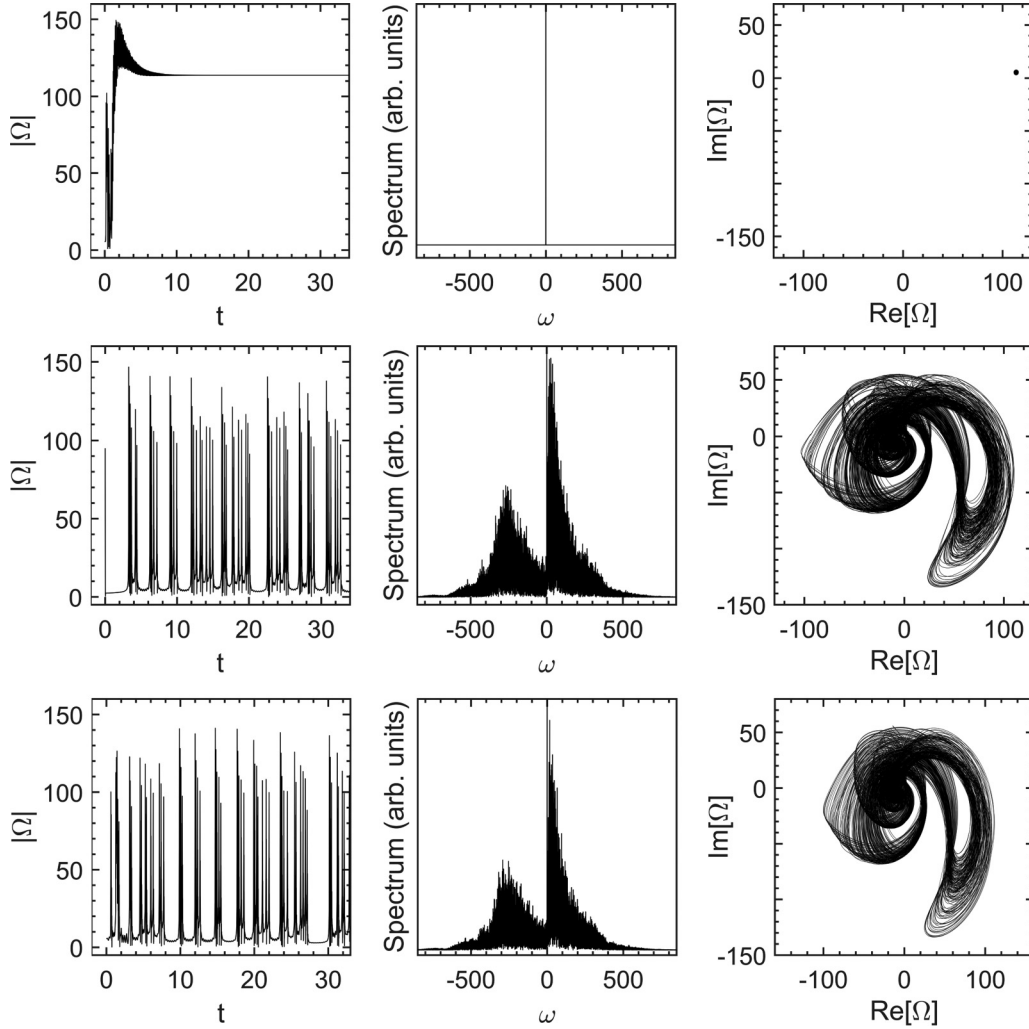


FIG. 8. Same as in Fig. 7, but for the case of the two-photon resonance ($\Delta_{21} = -\Delta_{32} = \Delta_B/2 = 25$) and two values of the external field magnitude $|\Omega_0|$. Top and middle rows: the system resides initially in the steady-state points ($|\Omega_0| = 95$, $|\Omega| = 5.5214$) and ($|\Omega_0| = 95.2$, $|\Omega| = 5.6121$), respectively. Bottom row: the system initially is in the ground state [$\rho_{11}(0) = 1$] and $|\Omega_0| = 95$.

aperiodic self-oscillations, and dynamical chaos. The origin of such a behavior is derived from the secondary field produced by the SQDs, which depends on the current state of SQDs. This can provide a strong enough positive feedback resulting finally in instabilities. If the secondary field is neglected, all above-mentioned effects disappear.

Below, we discuss the underlying nonlinearities giving rise to the exotic SQD supercrystal optical response. To this end, let us consider Eqs. (5d) and (5e). Substituting into Eqs. (5d) and (5e) the expression (5g) for the field Ω , one gets

$$\begin{aligned} \dot{\rho}_{21} = & -[i(\Delta_{21} - \Delta_L Z_{21}) + \frac{1}{2}\gamma - \gamma_R Z_{21}] \rho_{21} \\ & + \mu(\gamma_R + i\Delta_L) Z_{21} \rho_{32} + \mu(\gamma_R - i\Delta_L)(\rho_{21}^* + \mu\rho_{32}^*) \rho_{31} \\ & + \Omega_0(Z_{21} + \mu\rho_{31}), \end{aligned} \quad (9a)$$

$$\begin{aligned} \dot{\rho}_{32} = & -[i(\Delta_{32} - \mu^2 \Delta_L Z_{32}) + \frac{1}{2}(1 + \mu^2)\gamma - \mu^2 \gamma_R Z_{32}] \rho_{32} \\ & + \mu(\gamma_R + i\Delta_L) Z_{32} \rho_{21} - (\gamma_R - i\Delta_L)(\rho_{21}^* + \mu\rho_{32}^*) \rho_{31} \\ & + \Omega_0(\mu Z_{32} - \rho_{31}). \end{aligned} \quad (9b)$$

As is seen, these equations contain a number of nonlinear terms, however, a special attention should be paid to the first terms in the right-hand sides, which describe oscillations and decay of the off-diagonal density matrix elements ρ_{21} and ρ_{32} . Note that the secondary field results in an additional frequency detuning $\Delta_L Z_{21}$ and damping $\gamma_R Z_{21}$ for ρ_{21} and, respectively, $\mu^2 \Delta_L Z_{32}$ and $\mu^2 \gamma_R Z_{32}$ for ρ_{32} . These additional quantities depend on the corresponding population differences Z_{21} and Z_{32} . Thus, the following renormalizations are evident: $\Delta_{21} \mapsto \Delta_{21} - \Delta_L Z_{21}$ and $\gamma/2 \mapsto \gamma/2 - \gamma_R Z_{21}$ for the transition $2 \leftrightarrow 1$, and $\Delta_{32} \mapsto \Delta_{32} - \mu^2 \Delta_L Z_{32}$ and $(1 + \mu^2)\gamma/2 \mapsto (1 + \mu^2)\gamma/2 - \mu^2 \gamma_R Z_{21}$ for the transition $3 \leftrightarrow 2$.

Before the external field is switched on and the system is in the ground state, the population difference $Z_{21} = -1$, whereas $Z_{32} = 0$, because the states $|2\rangle$ and $|3\rangle$ are not populated. Accordingly, only the $(1 \leftrightarrow 2)$ transition experiences the above-mentioned renormalization, whereas the $(2 \leftrightarrow 3)$ transition does not. Thus, the initial values of the parameters of the $1 \leftrightarrow 2$ transition detuning and decay rate are $\Delta_{21} - |\Delta_L| \approx -|\Delta_L|$ and $\gamma/2 + \gamma_R \approx \gamma_R$, respectively (here we took into account that $|\Delta_L| \gg \Delta_{21}$ and $\gamma_R \gg \gamma/2$). All

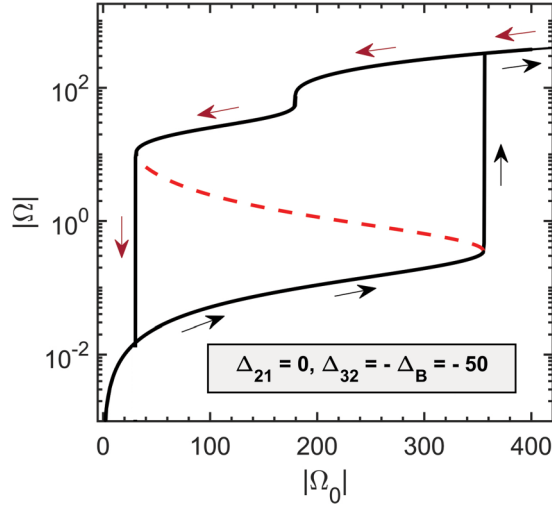


FIG. 9. Optical hysteresis of the total field magnitude $|\Omega|$ calculated by solving Eqs. (5a)–(5g) for the case of the one-photon resonance ($\Delta_{21} = 0$, $\Delta_{32} = -\Delta_B$) for $\Delta_B = 50$. The external field magnitude $|\Omega_0|$ was slowly swept back and forth across the multivalued part of the steady-state curve from Fig. 3, which is also shown for reference. The arrows indicate the sweep direction. All quantities are given in units of γ .

other resonance detunings and decay rates keep their bare values.

When the external field is switched on, the system starts to evolve, reaching finally the strong excitation regime. Alongside the dynamic shift $\Delta_L Z_{21}$ is increasing whereas the shift $\mu^2 \Delta_L Z_{32}$ is decreasing, which is driving the initially off-resonance situation toward a better resonance condition for both transitions. As a result, the redistribution of the level populations and the competition between transitions come into play creating necessary conditions for emerging instabilities (see Ref. [63] for more details). The system manifests the

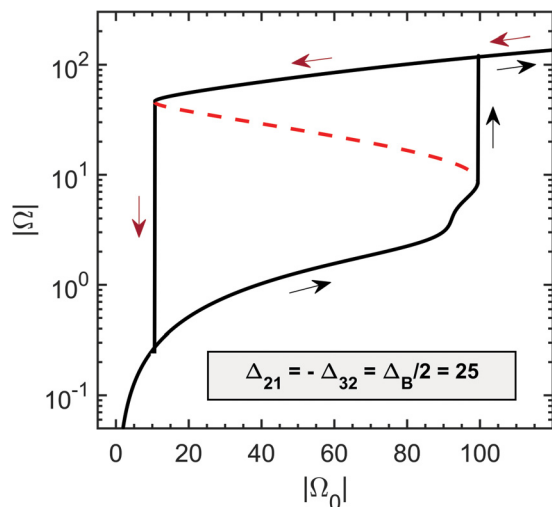


FIG. 10. Same as in Fig. 9, but for the case of the two-photon resonance ($\Delta_{21} = -\Delta_{32} = -\Delta_B/2$) with $\Delta_B = 50$.

bistability and hysteresis because the values of parameters Δ_L , γ_R are far above the bistability threshold [64,65].

Finally, as far as parameters are concerned, we would like to note that the model has so many of them that a complete study of the whole parameter space is hardly feasible. However, for particular systems, such as supercrystals comprising semiconductor quantum dots, some parameters are well known, in particular, the relaxation rates γ_{21} and γ_{32} and the relationship between them, while the biexciton binding energy Δ_B can vary by a factor of about 4–5. To demonstrate the possible impact of variations of the latter parameter, we presented results for a range of values of Δ_B (see Figs. 3 and 4).

The parameters Δ_L and γ_R (that are related to the secondary field) were kept fixed throughout the study. They have been estimated on the basis of experimental data presented in Fig. 1. In principle, both Δ_L and γ_R vary if the lattice constant of the supercrystal is different. We performed additional calculations (not presented here) for the values of these parameters twice as small as the ones used in this paper. As can be expected, the results were quantitatively different but the system was manifesting the same wide range of nontrivial dynamics. The robustness of the dynamics is related to the fact that Δ_L is the largest parameter in the problem and it therefore determines the optical response. Only when the value of Δ_L becomes comparable to that of Δ_B , the system becomes stable and all nontrivial dynamics scenarios disappear.

V. REFLECTANCE

In our analysis of the system's nonlinear response, we addressed the total field Ω acting on an emitter. Although this field can be measured by near-field techniques, it is less demanding to measure the reflected or transmitted fields. These are determined by the far-zone part of Ω and are given by the following expressions:

$$\Omega_{\text{refl}} = \gamma_R(\rho_{21} + \mu\rho_{32}), \quad (10a)$$

$$\Omega_{\text{tr}} = \Omega_0 + \gamma_R(\rho_{21} + \mu\rho_{32}). \quad (10b)$$

The reflectance R and transmittance T are then defined as

$$R = \left| \frac{\Omega_{\text{refl}}}{\Omega_0} \right|^2, \quad T = \left| \frac{\Omega_{\text{tr}}}{\Omega_0} \right|^2. \quad (11)$$

Let us first consider the linear regime of excitation and restrict ourselves to analyzing the steady-state reflectance. In this case, the major contribution to the secondary field comes from ρ_{21} which is given by

$$\rho_{21} = -\frac{\Omega_0}{\frac{1}{2}\gamma + \gamma_R + i(\Delta_{21} + \Delta_L)}. \quad (12)$$

Substituting Eq. (12) into (11), one obtains the following approximate expression for the reflectance R :

$$R = \left| \frac{\gamma_R}{\frac{1}{2}\gamma + \gamma_R + i(\Delta_{21} + \Delta_L)} \right|^2. \quad (13)$$

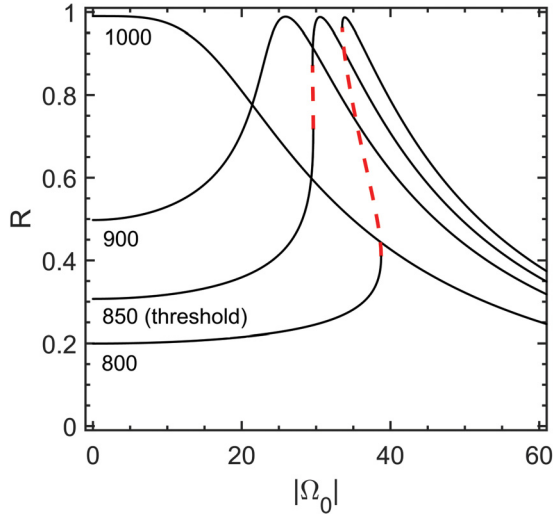


FIG. 11. The dependence of the steady-state reflectance R on the external field magnitude $|\Omega_0|$ calculated for different values of the detuning Δ_{21} in the vicinity of the renormalized resonance, $\Delta_{21} \leq -\Delta_L$. The results are calculated for the biexciton binding energy $\Delta_B = 50$, the values of Δ_{21} are given in the plot, herewith $\Delta_{21}^{\text{th}} = 850$ is the threshold detuning below which the reflectance becomes bistable. Dashed parts of the curves are unstable branches of the reflectance. All frequency-dimension quantities are given in units of γ .

It follows from the latter expression that for the range of relatively small detunings used so far in our calculations ($\Delta_{21} < 100$), the reflectance

$$R \approx \left| \frac{\gamma_R}{\Delta_L} \right|^2 \ll 1$$

because $|\Delta_L| \gg \Delta_{21}, \gamma_R$. Remarkably, if the excitation frequency is in the vicinity of the resonance renormalized by the near field, i.e., $|\Delta_{21} + \Delta_L| \ll \gamma_R$, the reflectance of the system is close to unity, $R \approx 1$. Thus, in this region of frequencies, the SQD supercrystal operates as a *perfect mirror*. It has been reported recently that an atomically thin mirror can be realized based on a monolayer of MoSe_2 [66,67]. SQD supercrystals represent yet another class of nanoscopically thin reflectors. The advantage of the latter, however, is that the properties of the SQD-based mirror can be controlled by the geometry and materials of the nanostructure.

Now, we turn to the nonlinear regime of reflectance in the vicinity of the renormalized resonance $\Delta_{21} \approx -\Delta_L$. We calculated the $|\Omega_0|$ dependence of the reflectance R for a set of detunings above the renormalized resonance $\Delta_{21} \leq -\Delta_L$. The results are presented in Fig. 11. The figure shows that at the exact resonance ($\Delta_{21} = -\Delta_L = 1000$), the reflectance decreases monotonously as the external field magnitude $|\Omega_0|$ increases. This behavior is explained by the dependence of the current detuning $\Delta'_{21} = \Delta_{21} - \Delta_L Z_{21}$ on the population difference [see Eq. (9a)]: as the system is being excited, it is driven away from the renormalized resonance and, consequently, reflects less.

If the system is initially out of the renormalized resonance ($\Delta_{21} \leq -\Delta_L$), the low-field reflectance is relatively small according to Eq. (13). As the system is being excited, it is

driven toward the resonance ($\Delta_{21} - \Delta_L Z_{21} \rightarrow 0$) and, at some $|\Omega_0|$, manifests again almost unity reflectance (Fig. 11). Furthermore, starting some critical value of Δ_{21} , namely, $\Delta_{21}^{\text{th}} = 850$ for the set of parameters used, the reflectance becomes three valued within some window of external field amplitudes, manifesting the optical bistability. The critical value $\Delta_{21}^{\text{th}} = 850$ is in a good agreement with the theoretical estimate made within the framework of an effective two-level model $\Delta_{21} = -\Delta_L - \sqrt{3}\gamma_R \approx 827$ [16]. A small deviation from the calculated value is probably due to the third biexciton level, a small admixture of which affects slightly the threshold value.

Finally, we note that the discussed reflectance properties are almost independent on the biexciton binding energy Δ_B , so our results should apply to a wide range of SDQ supercrystals.

VI. SUMMARY

We conducted a theoretical study of the optical response of a two-dimensional semiconductor quantum-dot supercrystal subjected to a monochromatic quasiresonant excitation. A constituent SQD was modeled as a three-level ladderlike system with the ground, one-exciton, and biexciton states. The set of parameters used in our study is typical for SQDs emitting in the visible range, such as CdSe and CdSe/ZnSe. We took into account the SQD dipole-dipole interaction within the framework of the mean field approximation.

To address the stationary response of the system, we developed an exact linear parametric method of solving the nonlinear steady-state problem which has multivalued solutions in all considered cases. Analyzing the Lyapunov exponents at the stationary characteristics, we found stable and unstable branches of the steady-state solutions. We provided a physical insight into the nature of the instabilities which have their origin in the competition between the ground-to-one exciton and one exciton-to-biexciton transitions, driven by the near-field SQD-SQD interactions. The stability analysis provided us with a solid starting point for further study of the system dynamics, which we first addressed qualitatively. To this end, we put forward a method to calculate the bifurcation diagram of the system which gives a general overview of possible system dynamics. It turned out that the 2D supercrystal optical response can manifest very different dynamics under a continuous wave (CW) excitation: periodic or aperiodic self-oscillations and probably chaotic behavior. The frequency of self-oscillations depends on the external field magnitude and, for the set of parameters used, falls in the THz region.

Our results suggest various applications of the 2D SQD supercrystals, such as an all-optical bistable switch, an ultrathin tunable bistable mirror, a tunable generator of trains of THz pulses (in self-oscillation regime), and as a noise generator (in chaotic regime). The intrinsic sensitivity of the optical response to the initial conditions in the chaotic regime could be of interest for information encryption [68]. All these findings make the considered system a promising candidate for practical applications in all-optical information processing and computing.

ACKNOWLEDGMENTS

A.V.M. acknowledge support from Spanish MINECO Grants No. MAT2013-46308 and No. MAT2016-75955.

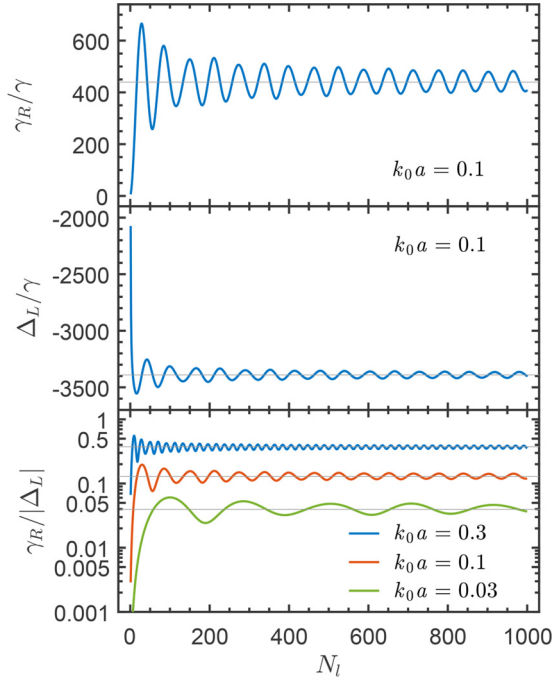


FIG. 12. The lateral size dependence of the collective radiation rate γ_R (upper plot), the near-zone dipole-dipole interaction of SQDs, Δ_L (middle plot), and the ratio $\gamma_R/|\Delta_L|$ (lower plot) calculated from Eqs. (6a) and (6b) for different values of $k_0 a$ (indicated in the plots). Thin horizontal lines are guides for the eye showing the asymptotic values of the oscillating functions.

I.V.R. acknowledges support from the Russian Foundation for Basic Research, Project No. 15-02-08369. A.V.M. is grateful to R. Noskov for useful discussions on bifurcation diagrams. We thank P. Á. Zapatero for prior collaboration on the topic.

APPENDIX A: NUMERICAL EVALUATION OF γ_R AND Δ_L

Here, we evaluate numerically γ_R and Δ_L , given by Eqs. (6a) and (6b), for a large square system ($N_x a, N_y a \gg \lambda$, $N_x = N_y = N_l$). In Fig. 12, we plotted γ_R , Δ_L , and the ratio $\gamma_R/|\Delta_L|$ against the system lateral size N_l for different values of $k_0 a$. As can be seen from the figure, these quantities manifest decaying oscillations around their asymptotic values, which reflect slow convergence of the sums that contain terms proportional to $|\mathbf{n}|^{-1}$. Comparing these data with the expected $(k_0 a)^{-2}$ scaling of γ_R and $(k_0 a)^{-3}$ scaling of Δ_L [which follow from Eqs. (6a) and (6b)] we obtained the approximate numerical formulas (8a) and (8b) which describe excellently all numerical data presented in Fig. 12.

APPENDIX B: SOLUTION OF THE STEADY-STATE PROBLEM

The steady-state problem is governed by the following set of equations:

$$\gamma \rho_{22} + \Omega \rho_{21}^* + \Omega^* \rho_{21} = 0, \quad (\text{B1a})$$

$$\mu \gamma \rho_{33} + \Omega \rho_{32}^* + \Omega^* \rho_{32} = 0, \quad (\text{B1b})$$

$$\Omega(\rho_{22} - \rho_{11}) - \left(i\Delta_{21} + \frac{\gamma}{2} \right) \rho_{21} + \mu \Omega^* \rho_{31} = 0, \quad (\text{B1c})$$

$$\mu \Omega(\rho_{33} - \rho_{22}) - \left[i\Delta_{32} + \frac{\gamma}{2}(1 + \mu^2) \right] \rho_{32} - \Omega^* \rho_{31} = 0, \quad (\text{B1d})$$

$$-\left(i\Delta_{31} + \frac{\gamma}{2} \mu^2 \right) \rho_{31} - \mu \Omega \rho_{21} + \Omega \rho_{32} = 0, \quad (\text{B1e})$$

$$\rho_{11} + \rho_{22} + \rho_{33} = 1. \quad (\text{B1f})$$

Thus, originally the system of nine nonlinear coupled equations for the density matrix elements should be solved to find the dependence of these elements and the total field Ω on the external field Ω_0 . The two fields are related by Eq. (5g) which we rewrite for convenience in the following form:

$$\Omega_0 = \Omega - (\gamma_R + i\Delta_L)(\rho_{21} + \mu\rho_{32}). \quad (\text{B2})$$

Traditionally, one or another numerical method of direct solution of the nonlinear system (B1a)–(B1f) is used. Below we propose a much more efficient and essentially linear parametric method to solve this nonlinear problem.

First, we note that Eqs. (B1a)–(B1f) and (B2) are invariant under the following phase transformation:

$$\rho_{21} \mapsto \rho_{21} e^{i\varphi}, \quad \rho_{32} \mapsto \rho_{32} e^{i\varphi}, \quad \rho_{31} \mapsto \rho_{31} e^{2i\varphi}, \quad (\text{B3a})$$

$$\Omega \mapsto \Omega e^{i\varphi}, \quad \Omega_0 \mapsto \Omega_0 e^{i\varphi}, \quad (\text{B3b})$$

where φ is an arbitrary phase. Second, the system of Eqs. (B1a)–(B1f) is linear in the density matrix elements if Ω is considered to be a parameter. Furthermore, Eq. (B3b) suggests that instead of (naturally) treating the external field amplitude Ω_0 as a real quantity, one can consider the total field amplitude Ω to be real (the phase of Ω can be chosen arbitrarily; the zero phase is just the most conventional choice).

Importantly, the system of Eqs. (B1a)–(B1f), as being a system of linear equations, can be solved analytically and the *unique* parametric dependence of all density matrix elements on Ω can be obtained. Then, Eq. (B2) provides the *unique* parametric dependence of the external field Ω_0 on the real total field Ω . The sought dependencies of the density matrix elements on the external field Ω_0 can then be obtained in the parametric way, varying the real Ω within an appropriate interval of values. Finally, to recover the “traditional” case, in which the external field amplitude Ω_0 is real, the transformations (B3) can be used with the phase $\varphi = -\arg \Omega_0$ given by

$$\varphi = -\arg[\Omega - (\gamma_R + i\Delta_L)(\rho_{21} + \mu\rho_{32})]. \quad (\text{B4})$$

To conclude, we note that our method of solving the nonlinear mean field steady-state equations for the density matrix elements is quite general and, therefore, can probably be applied to a broad class of similar systems.

- [1] N. I. Zheludev, *Science* **328**, 582 (2010).
- [2] N. I. Zheludev and Y. S. Kivshar, *Nat. Mater.* **11**, 917 (2012).
- [3] C. M. Soukoulis and M. Wegener, *Science* **330**, 1633 (2010).
- [4] Y. Liu and X. Zhang, *Chem. Soc. Rev.* **40**, 2494 (2011).
- [5] A. Alù, *Nat. Mater.* **15**, 1229 (2016).
- [6] A. S. Baimuratov, I. D. Rukhlenko, V. K. Turkov, A. V. Baranov, and A. V. Fedorov, *Sci. Rep.* **3**, 1727 (2013).
- [7] W. H. Evers, B. Goris, S. Bals, M. Casavola, J. de Graaf, R. van Roij, M. Dijkstra, and D. Vanmaekelbergh, *Nano Lett.* **13**, 2317 (2013).
- [8] M. P. Boneschanscher, W. H. Evers, J. J. Geuchies, T. Altantzis, B. Goris, F. T. Rabouw, S. A. P. van Rossum, H. S. J. van der Zant, L. D. A. Siebbeles, G. V. Tendeloo, I. Swart, J. Hilhorst, A. V. Petukhov, S. Bals, and D. Vanmaekelbergh, *Science* **344**, 1377 (2014).
- [9] A. V. Baranov, E. V. Ushakova, V. V. Golubkov, A. P. Litvin, P. S. Parfenov, A. V. Fedorov, and K. Berwick, *Langmuir* **31**, 506 (2015).
- [10] E. V. Ushakova, S. A. Cherevkin, A. P. Litvin, P. S. Parfenov, D.-O. A. Volgina, I. A. Kasatkin, A. V. Fedorov, and A. V. Baranov, *J. Phys. Chem. C* **120**, 25061 (2016).
- [11] W. Liu, X. Luo, Y. Bao, Y. P. Liu, G.-H. Ning, I. Abdelwahab, L. Li, C. T. Nai, Z. G. Hu, D. Zhao, B. Liu, S. Y. Quek, and K. P. Loh, *Nat. Chem.* **9**, 563 (2017).
- [12] Y. Ben-Aryeh, C. M. Bowden, and J. C. Englund, *Opt. Commun.* **59**, 224 (1986).
- [13] Y. Ben-Aryeh, C. M. Bowden, and J. C. Englund, *Phys. Rev. A* **34**, 3917 (1986).
- [14] S. M. Zakharov and E. A. Manykin, *Poverkhnost'* **2**, 137 (1988).
- [15] A. M. Basharov, *Zh. Eksp. Teor. Fiz.* **94**, 12 (1988) [*Sov. Phys. JETP* **67**, 1741 (1988)].
- [16] M. G. Benedict, A. I. Zaitsev, V. A. Malyshev, and E. D. Trifonov, *Opt. Spectrosc.* **68**, 473 (1990).
- [17] M. G. Benedict, V. A. Malyshev, E. D. Trifonov, and A. I. Zaitsev, *Phys. Rev. A* **43**, 3845 (1991).
- [18] A. N. Oraevsky, D. J. Jones, and D. K. Bandy, *Opt. Commun.* **111**, 163 (1994).
- [19] V. A. Malyshev and E. Conejero Jarque, *Opt. Express* **6**, 227 (2000).
- [20] H. Glaeske, V. A. Malyshev, and K.-H. Feller, *J. Chem. Phys.* **113**, 1170 (2000).
- [21] J. A. Klugkist, V. A. Malyshev, and J. Knoester, *J. Chem. Phys.* **127**, 164705 (2007).
- [22] R. F. Malikov and V. A. Malyshev, *Opt. Spectrosc.* **122**, 955 (2017).
- [23] A preliminary study of the quantum-dot supercrystal's optical response has been recently reported in Refs. [71,72].
- [24] A. A. Andronov, A. A. Vitt, and S. E. Khaikin, *Theory of Oscillators* (Pergamon Press, New York, 1966).
- [25] J.-P. Eckmann and D. Ruelle, *Rev. Mod. Phys.* **57**, 617 (1985).
- [26] J. Guckenheimer and P. Holmes, *Nonlinear Oscillations, Dynamical Systems and Bifurcations of Vector Fields* (Springer, Berlin, 1986).
- [27] Y. I. Neimark and P. S. Landa, *Stochastic and Chaotic Oscillations* (Springer, Dordrecht, 1992).
- [28] E. Ott, *Chaos in Dynamical Systems* (Cambridge University Press, Cambridge, 1993).
- [29] V. S. Afrajmovich, Y. S. Il'yashenko, and L. P. Shil'nikov, in *Dynamical Systems V: Bifurcation Theory and Catastrophe Theory*, edited by V. I. Arnol'd (Springer, Berlin, 1994).
- [30] K. T. Alligood, T. D. Sauer, and J. A. Yorke, *Chaos: An Introduction to Dynamical Systems* (Springer, Berlin, 1996).
- [31] A. Katok and B. Hasselblatt, *Introduction to the Modern Theory of Dynamical Systems* (Cambridge University Press, Cambridge, 1997).
- [32] Y. A. Kuznetsov, *Elements of Applied Bifurcation Theory* (Springer, Berlin, 2004).
- [33] S. Wieczorek, B. Krauskopf, T. B. Simpson, and D. Lenstra, *Phys. Rep.* **416**, 1 (2005).
- [34] S. Stuffer, P. Machnikowski, P. Ester, M. Bichler, V. M. Axt, T. Kuhn, and A. Zrenner, *Phys. Rev. B* **73**, 125304 (2006).
- [35] G. Jundt, L. Robledo, A. Högele, S. Fält, and A. Imamoglu, *Phys. Rev. Lett.* **100**, 177401 (2008).
- [36] B. Gerardot, D. Brunner, P. Dalgarno, K. Karrai, A. Badolato, P. Petroff, and R. Warburton, *New J. Phys.* **11**, 013028 (2009).
- [37] G. Lindblad, *Commun. Math. Phys.* **48**, 119 (1976).
- [38] K. Blum, *Density Matrix: Theory and Applications*, 3rd ed. (Springer, Berlin, 2012).
- [39] A. I. Zaitsev, V. Malyshev, and E. D. Trifonov, *Zh. Eksp. Teor. Fiz.* **84**, 475 (1983) [*Sov. Phys. JETP* **57**, 285 (1983)].
- [40] M. G. Benedict, A. M. Ermolaev, V. A. Malyshev, I. V. Sokolov, and E. D. Trifonov, *Super-radiance: Multiatomic Coherent Emission* (IOP Publishing, Bristol, 1996).
- [41] M. Born and E. Wolf, *Principles of Optics* 6th ed. (Pergamon Press, Oxford, 1980).
- [42] R. Friedberg, S. R. Hartmann, and J. T. Manassah, *Phys. Rep.* **7**, 101 (1973).
- [43] F. A. Hopf, C. M. Bowden, and W. H. Louisell, *Phys. Rev. A* **29**, 2591 (1984).
- [44] V. Malyshev and E. Conejero Jarque, *J. Opt. Soc. Am. B* **14**, 1167 (1997).
- [45] V. Malyshev and E. Conejero Jarque, *Opt. Spectrosc.* **82**, 582 (1997).
- [46] M. L. Glasser, *J. Math. Phys.* **14**, 409 (1972).
- [47] P. L. Christiansen, Y. B. Gaididei, M. Johansson, K. O. Rasmussen, V. K. Mezentsev, and J. J. Rasmussen, *Phys. Rev. B* **57**, 11303 (1998).
- [48] R. H. Dicke, *Phys. Rev.* **93**, 99 (1954).
- [49] C. Mai, A. Barrette, Y. Yu, Y. G. Semenov, K. W. Kim, L. Cao, and K. Gundogdu, *Nano Lett.* **14**, 202 (2014).
- [50] K. F. Mak and J. Shan, *Nat. Photon.* **10**, 216 (2016).
- [51] E. N. Lorenz, *J. Atmos. Sci.* **20**, 130 (1963).
- [52] I. Shimada and T. Nagashima, *Prog. Theor. Phys.* **61**, 1605 (1979).
- [53] G. Benettin, L. Galgani, A. Giorgilli, and M. Strelcyn, *Meccanica* **15**, 9 (1980).
- [54] G. Benettin, L. Galgani, A. Giorgilli, and M. Strelcyn, *Meccanica* **15**, 21 (1980).
- [55] A. Wolf, J. B. Swift, H. Swinney, and J. A. Vastano, *Physica D (Amsterdam)* **16**, 285 (1985).
- [56] L. Dieci and E. S. Van Vleck, *Appl. Numer. Math.* **17**, 275 (1995).
- [57] L. Dieci, R. D. Russell, and E. S. Van Vleck, *SIAM J. Numer. Anal.* **34**, 402 (1997).
- [58] J. Scales and E. S. Van Vleck, *J. Comput. Phys.* **133**, 27 (1997).
- [59] P. Frederickson, J. L. Kaplan, E. D. Yorke, and J. A. Yorke, *J. Diff. Equ.* **49**, 185 (1983).
- [60] J. L. Kaplan and J. A. Yorke, in *Functional Differential Equations and Approximation of Fixed Points*, edited by H.-O. P.-O.

- Walther, *Lecture Notes in Mathematics* Vol. 730 (Springer, Berlin, 1979), pp. 204–227.
- [61] Y.-C. Lai and T. Tél, *Transient Chaos. Complex Dynamics in Finite-time Scales* (Springer, Berlin, 2011).
- [62] T. Tél, *Chaos* **25**, 097619 (2015).
- [63] B. S. Nugroho, A. A. Iskandar, V. A. Malyshev, and J. Knoester, *J. Opt.* **19**, 015004 (2017).
- [64] R. Friedberg, S. R. Hartmann, and J. T. Manassah, *Phys. Rev. A* **39**, 3444 (1989).
- [65] A. V. Malyshev, *Phys. Rev. A* **86**, 065804 (2012).
- [66] P. Back, S. Zeytinoglu, A. Ijaz, M. Kroner, and A. Imamoğlu, *Phys. Rev. Lett.* **120**, 037401 (2018).
- [67] G. Scuri, Y. Zhou, A. A. High, D. S. Wild, C. Shu, K. De Greve, L. A. Jauregui, T. Taniguchi, K. Watanabe, P. Kim, M. D. Lukin, and H. Park, *Phys. Rev. Lett.* **120**, 037402 (2018).
- [68] T. Gao and Z. Chen, *Phys. Lett. A* **372**, 394 (2008).
- [69] R. A. Vlasov, A. M. Lemeza, and M. G. Gladush, *J. Appl. Spectrosc.* **80**, 698 (2013).
- [70] R. A. Vlasov, A. M. Lemeza, and M. G. Gladush, *Las. Phys. Lett.* **10**, 045401 (2013).
- [71] R. F. Malikov, I. V. Ryzhov, and V. A. Malyshev, *EPJ Web Conf.* **161**, 02014 (2017).
- [72] V. A. Malyshev, P. A. Zapatero, A. V. Malyshev, R. F. Malikov, and I. V. Ryzhov, *J. Phys.: Conf. Ser.* **1220**, 012006 (2019).
- [73] A. V. Malyshev and V. A. Malyshev, *Phys. Rev. B* **84**, 035314 (2011).
- [74] R. D. Artuso and G. W. Bryant, *Phys. Rev. B* **87**, 125423 (2013).